



RESEARCH ARTICLE



Molecular modeling studies on the interactions of 7-methoxytacrine-4-pyridinealdoxime, 4-PA, 2-PAM, and obidoxime with VX-inhibited human acetylcholinesterase: a near attack conformation approach

Jorge Alberto Valle da Silva^a , Eugenie Nepovimova^b, Teodorico Castro Ramalho^{b,c}, Kamil Kuca^b and Tanos Celmar Costa França^{a,b} 

^aLaboratory of Molecular Modeling Applied to the Chemical and Biological Defense (LMCBD), Department of Chemical Engineering, Military Institute of Engineering, Rio de Janeiro/RJ, Brazil; ^bFaculty of Science, Department of Chemistry, University of Hradec Kralove, Hradec Kralove, Czech Republic; ^cLaboratory of Molecular Modeling, Chemistry Department, Federal University of Lavras, Lavras, Brazil

ABSTRACT

7-methoxytacrine-4-pyridinealdoxime (7-MEOTA-4-PA, named hybrid 5C) is a compound formerly synthesized and evaluated *in vitro*, together with 4-pyridine aldoxime (4-PA) and commercial reactivators of acetylcholinesterase (AChE). This compound was designed with the purpose of being a prophylactic reactivator, capable of interacting with different subdomains of the active site of AChE. To investigate these interactions, theoretical results from docking were first compared with experimental data of hybrid 5C, 4-PA, and two commercial oximes, on the reactivation of human AChE (*HssAChE*) inhibited by VX. Then, further docking studies, molecular dynamics simulations, and molecular mechanics Poisson–Boltzmann surface area calculations, were carried out to investigate reactivation performances, considering the near attack conformation (NAC) approach, prior to the nucleophilic substitution mechanism. Our results helped to elucidate the interactions of such molecules with the different subdomains of the active site of *HssAChE*. Additionally, NAC poses of each oxime were suggested for further theoretical studies on the reactivation reaction.

ARTICLE HISTORY

Received 1 January 2019
Revised 10 April 2019
Accepted 11 April 2019

KEYWORDS

Acetylcholinesterase; VX; molecular modeling; NAC; 7-MEOTA-4-PA


1. Introduction

2-pyridinium methyl aldoxime, known as pralidoxime or 2-PAM, was the first commercial antidote for the treatment of lethal intoxications by organophosphates (OP)^{1,2}, being first administered in 1956, against parathion poisoning in Japan³. Since then, thousands of oximes, including the commercial bis-pyridinium aldoximes obidoxime and asoxime (HI-6), have been synthesized and evaluated. However, all these molecules were designed with the sole purpose of entering and removing the OP from the active site of the enzyme acetylcholinesterase (AChE), which is responsible for the hydrolysis of the neurotransmitter acetylcholine (ACh), and also the main molecular target of the OPs^{2,4}. Recently a new approach in the design of antidotes against OPs has proposed the design of novel prophylactic enzymatic reactivators through the conjugation of the 4-pyridine aldoxime (4-PA) to a peripheral site ligand (PSL) capable of binding to the peripheral anionic site (PAS) of AChE^{2,5}. Nepovimova et al.⁶ designed a novel hybrid reactivator bearing 7-methoxytacrine (7-MEOTA) as a PSL linked to 4-PA through a 5-carbon spacer (Figure 1). Ideally, this drug, named hybrid 5C by Nepovimova et al.⁶, would act in a prophylactic reversible inhibition of human AChE (*HssAChE*) thanks to the occupancy of the 7-MEOTA moiety at the PAS, and the action of the 4-PA moiety in the catalytic anionic site (CAS; Figure 2). In case intoxication occurs, the 4-PA fragment would

reactivate the phosphorylated *HssAChE*, acting as an antidote⁶. Figure 1 summarizes former experimental results through *in vitro* tests regarding the reactivation of VX-inhibited *HssAChE* versus *HssAChE* inhibition by hybrid 5C^{6,8}. This compound was evaluated together with the commercial reactivators 2-PAM and obidoxime, as well as 4-PA (Figure 1). According to Nepovimova et al.⁶, even though the 7-MEOTA moiety has a relatively strong capacity of enzymatic inhibition, hybrid 5C was capable of reactivating VX-inhibited *HssAChE* better than obidoxime.

The reactivation reaction of OP-inhibited *HssAChE* is the primary action of pyridinium aldoxime-based drugs and the most relevant mechanism for therapy against OP poisoning^{1,9}. It is not a catalytic process and may proceed via the scheme described in Figure 2. After the aldoxime moiety approaches the phosphorylated Ser203 at the CAS, it may form a reversible pentacoordinate transition state (TS), followed by the displacement of the phosphorylated aldoxime (*OPAlDox*) and consequent reactivation of *HssAChE*^{1,5}. The kinetic properties of this mechanism can be quantified *in vitro* by determination of the constants shown in Figure 2. The dissociation constant (K_D) is inversely proportional to the affinity of the aldoxime (ligand) to the phosphorylated *HssAChE* (receptor), while the rate constant (k_r) indicates the aldoxime reactivity, and the rate constant ($k_{OPAlDox}$) is related to the re-inhibition of the reactivated *HssAChE* by a sufficiently stable *OPAlDox*^{1,9}.

CONTACT Tanos Celmar Costa França  tanos@ime.eb.br; Kamil Kuca  kamil.kuca@uhk.cz  Faculty of Science, Department of Chemistry, University of Hradec Kralove, Hradec Kralove 50003, Czech Republic

 Supplemental data for this article can be accessed [here](#).

© 2019 The Author(s). Published by Informa UK Limited, trading as Taylor & Francis Group.

This is an Open Access article distributed under the terms of the Creative Commons Attribution License (<http://creativecommons.org/licenses/by/4.0/>), which permits unrestricted use, distribution, and reproduction in any medium, provided the original work is properly cited.

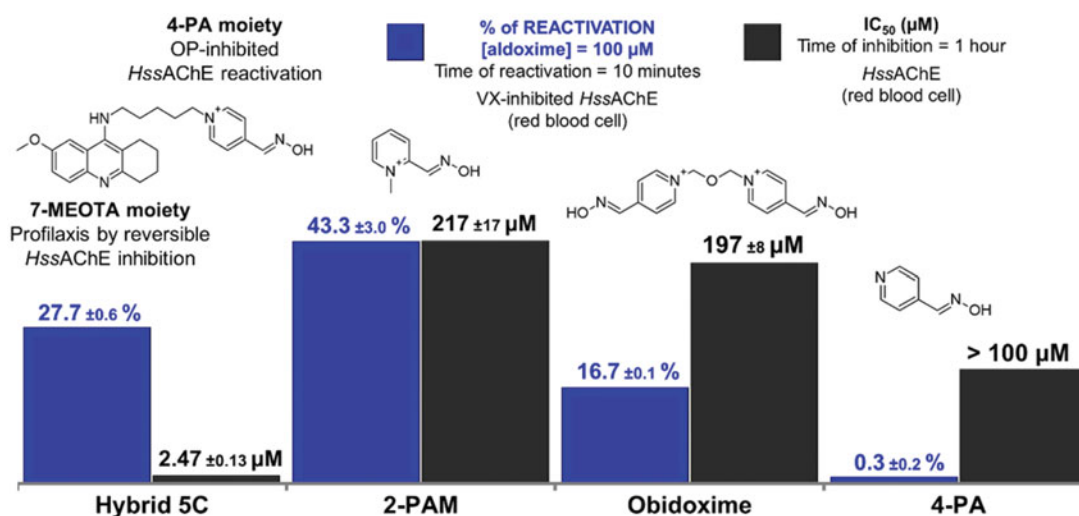


Figure 1. Molecular structures of some aldoximes and its experimental results for VX-inhibited *HssAChE*, as reported by Nepovimova et al.⁶

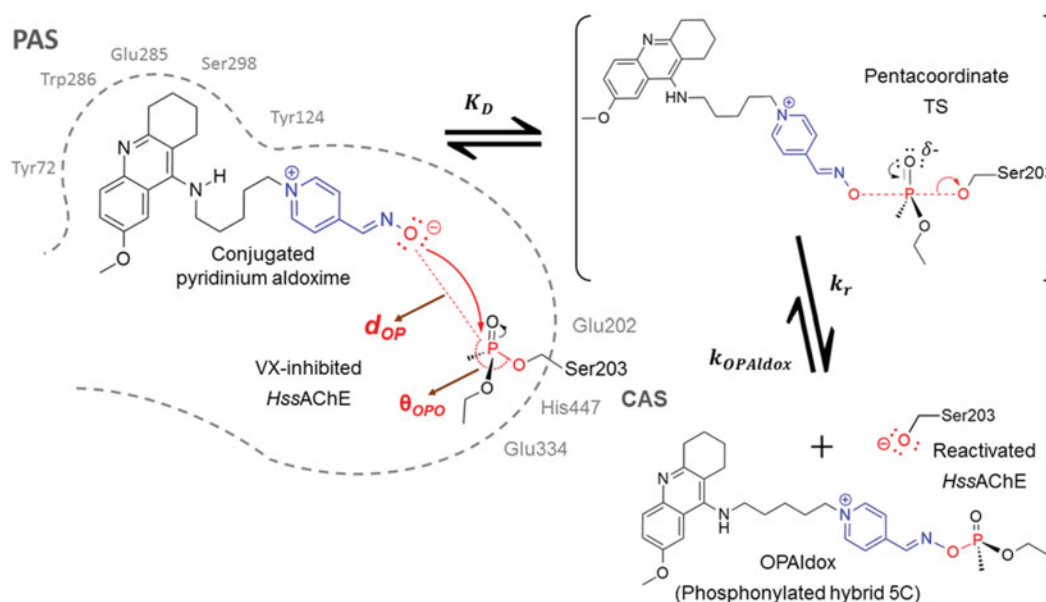


Figure 2. NAC approach representation. Interactions of conjugated pyridinium aldoximes with the PAS and CAS of VX-inhibited *HssAChE* just before the reactivation reaction^{1,5,7}.

In this work, techniques of molecular modelling were applied within limits of docking algorithm¹⁰ and classical molecular dynamics (MD)⁷, considering the near attack conformation (NAC) approach¹¹ (Figure 2), to analyse interactions of the complexes *HssAChE*/VX/aldoxime studied by Nepovimova et al.⁶, and their thermodynamic contributions for reactivation of *HssAChE*⁷. NAC is defined here as the conformation of the oxime with distance between the O of the oxime group ($-C=NOH$) and the P of the OP (d_{OP}) near to van der Waals contact, and the angle amongst the O of the oxime group, the P of the OP-Ser203 adduct, and the O of Ser203 (θ_{OPO}), as aligned as possible. Resembling the bonds to be formed and broken in the transition state (TS) of a S_N2 reaction¹¹. Initially, poses were computed and evaluated through docking studies. Then, one pose at the NAC for each oxime was selected and submitted to rounds of molecular dynamics (MD) simulations to compute frames with atomic trajectories regarding the dynamic behaviour of ligands. Finally, molecular mechanics Poisson-Boltzmann surface area (MM-PBSA) calculations were used to computing the binding energies of the calculated frames

and supporting the selection of refined NACs for future thermodynamics and kinetics studies.

2. Methodology

The docking studies were carried out assuming that the S_N2 mechanism⁷ takes place within the narrow gorge shaped active center of *HssAChE* where PAS and CAS are located at the entrance and bottom, respectively^{4,5}. Accordingly, computed poses were selected under the geometrical limitation of a nucleophilic attack in a NAC docked within the gorge, as illustrated in Figure 2. After, a strategic pose was selected as ligand for the MD simulations. Obidoxime and hybrid 5C were also studied as oximates ($-C=NO^-$)^{4,5,12,13}, once deprotonation of the $-C=NOH$ group may happen, under physiologic conditions, in the pathway toward the NAC⁵. The blue lines in Figure 3 show the energy profile suggested as strategy employed in this work to figure out a refined NAC needed to run the further steps represented by the black lines in Figure 3. These steps correspond to deeper theoretical

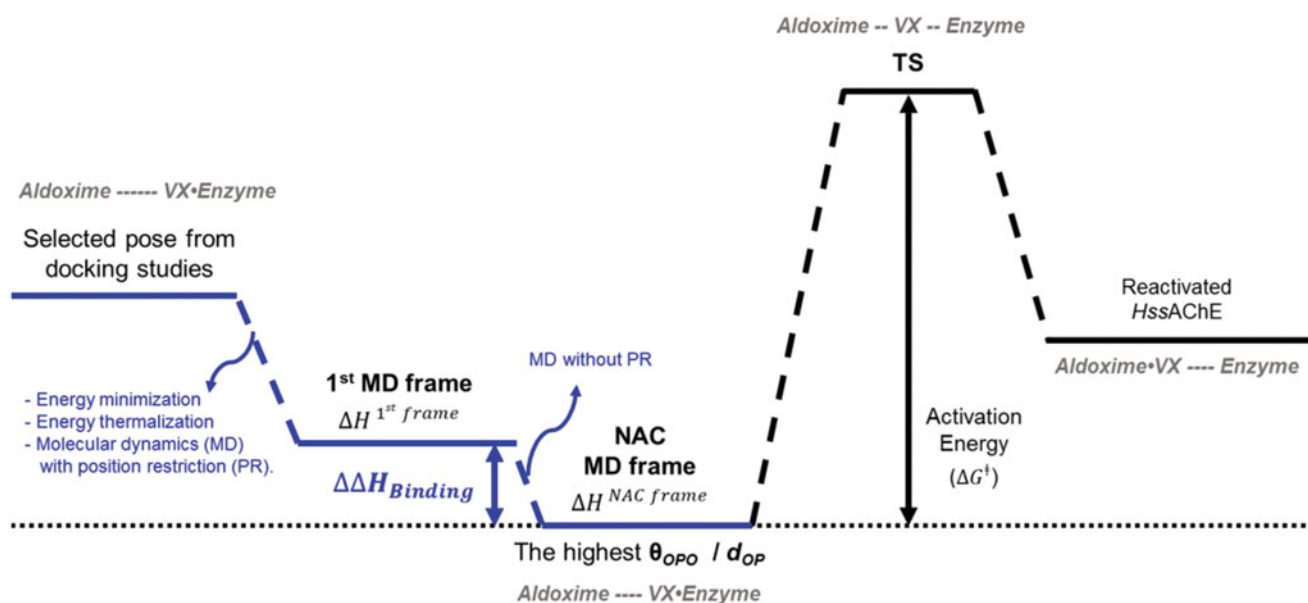


Figure 3. Energy profile for the whole process of *HssAChE* reactivation. NAC: Near Attack Conformation; TS: Transition State.

studies through quantum mechanics (QM) and QM associated with molecular mechanics (QM/MM) methods. These studies, besides being useful to validate the model presented in this work, will also contribute to the elucidation of the (still not fully understood) mechanism of reactivation of AChE by oximes.

2.1. Modeling of the oximes

Protonation states of the oximes shown in Figure 1 were estimated through the Chemicalize web-based resource supported by ChemAxon Ltd. at <https://chemicalize.com/welcome14>. This server predicts aqueous ionization constants (pKa) of organic molecules based mainly on empirically calculated partial charges and parameterized H-bonds. After that, the molecular structures were modeled with the software PC Spartan Pro 1.0.5¹⁴, according to the predicted protonation states, and optimized with the Merck Molecular Force Field (MMFF94)¹⁵. Then, their partial atomic charges were calculated through the semi-empirical quantum chemistry Austin Model 1 (AM1) method¹⁶ combined with the restrained electrostatic potential (RESP) model¹⁷.

2.2. Modeling of the receptor

The model of VX-inhibited *HssAChE* was built through mutations and corrections in the crystal structure of *Mus musculus* AChE (*MmAChE*), inhibited by tabun (GA) and complexed with HI-6, available in the Protein Data Bank (PDB) website <http://www.rcsb.org/pdb>¹⁸, under the code 3ZLV¹⁹. The structures of target (*MmAChE*) and template (*HssAChE*) present 88.60% of homological identity, with 100% of conserved residues at the active sites. Using the software Discovery Studios® Visualizer 4.5 (DS® Vis 4.5)²⁰, the complex *MmAChE*/GA/HI-6 was aligned to the FASTA sequence of *HssAChE* available at the UniProtKB data bank^{21,22}, under the code UniProtKB P22303²³. After, the complex *MmAChE*/GA/HI-6 was manually corrected and transformed into the model *HssAChE*/VX/HI-6, keeping all water molecules from the crystallographic structure conserved. Finally, the molecular geometry of the model was optimized through the revised version of the Chemistry at HARvard Macromolecular Mechanics (CHARMM) all-atom protein force field²⁴, named CHARMM3626. The parameters

of this version represent an improved model of the potential energy surface of proteins for modelling and simulation of protein dynamics in pharmacological applications. The functionally relevant conformational changes consist in newly optimized backbone torsional correction CMAP and side-chain dihedral potentials^{24,25}. The first new potential was refined from experimental data on small peptides and the second one, with quantum mechanical energies from dipeptides and nuclear magnetic resonance data from unfolded proteins²⁴. In addition, the new dihedral correction CMAP potential includes revised Lennard–Jones parameters for aliphatic hydrogens²⁶ as well as new parameters for tryptophan²⁷, being able to over stabilize helices, providing more reasonable results for the helix formed in a peptide²⁴.

2.3. Docking studies

Prior to docking calculations, a re-docking procedure was performed to validate the protocol used. For that, the entire modelled complex *HssAChE*/VX/HI-6 was imported to the software Molegro Virtual Docker® (MVD®) 6.0²⁸ and the crystallographic structure of HI-6 was docked over itself. The best pose from re-docking was chosen by considering the standard cartesian root-mean-square deviation (RMSD) values as well as the ligand–receptor interactions, in comparison with the crystallographic conformation of HI-6¹⁹. For the subsequent docking studies, the 3D structures of the ligands were also imported into MVD® 6.0²⁸. The cavity was detected by molecular surface with a probe size = 0.16 nm²⁰ from the corrected crystallographic conformation of HI-6¹⁹. Using grid resolution = 0.03 nm, scaling factor = 0.5, and crossover rate = 0.9, 450 poses were generated from 15 runs, combining population sizes of 30, 50, 100, 200, and 300, with maximum iterations of 2000, 2500, and 3000. For analysis of the selected poses, interactions with the side-chains of amino acids were computed with interatomic distances up to 0.5 nm. The calculated volume and surface of the *HssAChE*/VX cavity were, respectively, 0.326 nm³ and 5.491 nm², and the binding site was restricted to a sphere with a radius of 1.5 nm, centered at coordinates $x = 3.306$ nm, $y = 2.202$ nm, and $z = 1.000$ nm.

Both re-docking and docking calculations were performed through the hybrid search MolDock algorithm together with the

cavity prediction algorithm²⁹. The docking energies were calculated in terms of MolDock Score (E_{SCORE}), defined by Equation (1)²⁸.

$$E_{\text{SCORE}} = E_{\text{inter}} + E_{\text{intra}} \quad (1)$$

Where E_{inter} is the ligand–protein interaction energy that takes into account steric approximations between atoms, based on van der Waals (vdW) interactions, a specific potential for H-bonds, and electrostatic interactions between charged atoms. E_{intra} is the ligand internal energy involving pairs of atoms of the ligand (except those connected by two bonds), bond torsional angles, and penalties for distances between two heavy atoms smaller than 0.20 nm²⁸. A crucial parameter adopted was the percentage of selected poses at the NAC, calculated from the MolDock algorithm. Accordingly, poses were chosen, considering the distance $d_{\text{OP}} < 0.9$ nm and the angle $140^\circ < \theta_{\text{OPO}} < 180^\circ$, meant to provide an orbital overlapping consistent with the penta-coordinate TS shown in Figure 2^{5,30–33}. Considering the random nature of the functions of the MolDock algorithm to generate initial populations and subsequent generations of poses until the final 30 per run²⁸, the % of selected poses could be related to the probability of the aldoxime to be in favorable conditions of successfully reactivating the enzyme, and the highest % of selected poses might be assigned to the most promising reactivator. Therefore, the best pose of each compound was selected according to the highest value of the ratio $\theta_{\text{OPO}}/d_{\text{OP}}$, presenting the nearest (lowest d_{OP}) and most aligned (θ_{OPO} closest to 180°) position.

2.4. MD Simulations

The best pose of each ligand selected from the docking studies was submitted to rounds of MD simulations, using the GROMACS 5.1.4 computational package^{34,35}, with the OPLS/AA (Optimized Potentials for Liquid Simulations/All Atoms) force field³⁶, to evaluate its dynamical behaviours, stability, and interactions inside the complex *HssAChE/VX*¹⁰. Each pose was previously parameterized by the AnteChamber PYthon Parcer InterfacE (ACPYPE) algorithm³⁷ to generate files of topology with parameters to be recognized by the OPLS/AA force field³⁶. In addition, atomic mass and atomic partial charges of ligands were previously calculated by the software semi-empirical quantum chemistry (SQM) using the AnteChamber algorithm^{38,39}. H-bond interactions were computed considering interatomic distances between heavy atoms (O and N) up to 0.4 nm, and their angle with hydrogen up to 40°.

Mulliken atomic partial charges of the ligands were calculated at AM1 level¹⁶ with bond charge corrections (BCC) to reproduce them as RESP¹⁷. Some atomic mass and OPLS/AA parameters data of such output topology files were corrected by the MKTOP algorithm⁴⁰. Short-range vdW and electrostatic interactions were considered up to a cutoff = 1.0 nm and long-range electrostatic interactions were calculated using the Particle Mesh Ewald (PME) method⁴¹. The systems were subjected to energy minimizations to accommodate the water molecules and avoid overlapping of vdW radius. As before^{42–44}, different algorithms with a maximum of 20,000 steps each one, were used as follows: two steepest descent minimizations, one with position restriction (STPR) up to a maximum force of 104.6 kJ mol⁻¹ nm⁻¹ and another without PR (ST) up to 209.2 kJ mol⁻¹ nm⁻¹; conjugate gradients (CG) minimization, up to 104.6 kJ mol⁻¹ nm⁻¹; and L-BFGS, a quasi-Newton–Raphson-based method, up to 41.84 kJ mol⁻¹ nm⁻¹. After, the isothermal-isochoric (NVT) and the subsequent isothermal-isobaric (NPT) ensembles were simulated to equilibrate pressure and volume of the system. Physiologic conditions were considered with $T = 37^\circ\text{C}$

and $P = 100$ kPa, PR for the inhibited protein, leap-frog integrator, V-rescale thermostat modified from Berendsen⁴⁵ for temperature coupling, Parrinello–Rahman barostat⁴⁶ for pressure coupling, 2 fs of integration step, and 100 ps of simulation. Finally, the systems were subjected to 500 ps of MD simulation with PR for all atoms, except the water molecules, to ensure a balance of the solvent around the protein, and then, followed by 50 ns of MD production without restraints. Such MD simulations were run with leap-frog integrator, 2 fs of integration step, and V-rescale thermostat. Trajectories and energy data of the whole system and all its particles were obtained at every 100 ps of simulation to calculate properties such as total energy, RMSD, average number of H-bonds, and atomic distances. Output files from MD simulations were visualized with XMGRACE 5.1.25, Visual Molecular Dynamics (VMD) 1.9.3⁴⁷, PyMOL 1.3, Molecular Graphics System 2010 Schrodinger, LLC⁴⁸, and DS[®] Vis 4.5²⁰. The MD simulations were run in cubic boxes fulfilled by TIP4P water molecules⁴⁹ with distance solute-wall of 1.2 nm, including periodic boundary conditions (PBC).

2.5. Binding energy

Integrated to the MD simulations, biomolecular interaction energies and the contributions per amino acid residue were estimated to look over key residues and their roles in the stabilization of the ligands inside the complex *HssAChE/VX*. In that case, the MM-PBSA method^{50–53} was used through the *g_mmpbsa* software⁵² integrated with GROMACS 5.1.4^{34,35}, to analyse the evolution of the total binding energies as a function of time. In MM-PBSA calculations, solvation properties are assessed by combining contributions to the free energy of the ligand–receptor system ($\Delta G_{\text{Binding}}$)^{52–54}, expressed in Equation (2).

$$\Delta G_{\text{Binding}} = \Delta H_{\text{Binding}} - T\Delta S = \Delta E_{\text{MM}} + \Delta G_{\text{Solvation}} - T\Delta S \quad (2)$$

Where each term corresponds to the variation of the respective energies from the aldoxime and the *HssAChE/VX* complex, calculated separately, and the complex *HssAChE/VX*/aldoxime, calculated as a whole system^{52–54}. $\Delta H_{\text{Binding}}$ and $T\Delta S$ refer to the contributions of enthalpy and entropy, respectively. ΔE_{MM} includes bonded terms (such as bond, angle, and torsion energies) as well as no bonded terms (such as vdW and electrostatic interactions)⁵².

Focused on just comparing energies of biomolecular interactions, only variations of enthalpy were considered to be binding energies in MM-PBSA calculations ($\Delta H_{\text{MM-PBSA}}$)⁵², simplifying Equations (2) to (3).

$$\Delta H_{\text{Binding}} = \Delta H_{\text{MM-PBSA}} = \Delta E_{\text{MM}} + \Delta G_{\text{Polar}} + \Delta G_{\text{Nonpolar}} \quad (3)$$

Where solvation effects are accounted for ΔG_{Polar} and $\Delta G_{\text{Nonpolar}}$, using an implicit solvation model^{55–57}. ΔG_{Polar} , estimated by solving the Poisson–Boltzmann equation⁵⁸, is related to the electrostatic interaction between solute and solvent so that the polar surface is associated with the charge distribution of the solute. Binding energies were then computed individually for each residue to analyze its contribution for the biomolecular interaction, according to Equations (4)–(6).

$$\langle \Delta H_{\text{Binding}} \rangle = \sum \langle \Delta H_{\text{Residue}} \rangle \quad (4)$$

$$\langle \Delta H_{\text{Residue}} \rangle = \langle E_{\text{MM}} \rangle + \langle \Delta G_{\text{Polar}} \rangle + \langle \Delta G_{\text{Nonpolar}} \rangle \quad (5)$$

$$\Delta \Delta H_{\text{Binding}} = \Delta H^{\text{NACframe}} - \Delta H^{\text{first frame}} \quad (6)$$

Where $\langle \Delta H_{\text{Residue}} \rangle$ is the average of the binding energies $\Delta H_{\text{Residue}}$ calculated for each residue through Equation (3), per new frame. Likewise, $\Delta \Delta H_{\text{Binding}}$ represents the total binding energy to achieve

the NAC during the MD simulation. $\Delta H^{\text{NACframe}}$ is the $\Delta H_{\text{Binding}}$ calculated by Equation (3) just for the NAC frame, selected through the highest ratio $\theta_{\text{OPO}}/d_{\text{OPO}}$. $\Delta H^{\text{first frame}}$ is the $\Delta H_{\text{Binding}}$ also calculated through Equation (3), just for the first frame of the MD simulation, which was obtained from steps of energy minimization and thermalization of the best-evaluated pose selected by docking studies, as shown in Figure 3.

Dielectric constants of 2, 80, and 1 were considered for solute (*HssAChE/VX/ligand*), solvent (water) and vacuum, respectively^{50,52}. $\Delta G_{\text{Nonpolar}}$ includes repulsive and attractive forces between solute (generated by cavity formation) and solvent (generated by vdW interactions)^{56,57}. The Solvent Accessible Surface Area (SASA) was the only model used for $\Delta G_{\text{Nonpolar}}$ calculation^{50,52,56,57}, with surface tension simulated in $2.26778 \text{ kJ mol}^{-1} \text{ nm}^{-2}$, and probe radius = 0.14 nm. The number of grid points per area unit was set to 10 for ΔG_{Polar} and 20 for $\Delta G_{\text{Nonpolar}}$. New frames were calculated by an autocorrelation function from the ones obtained through MD simulations^{50,52} so each term of Equation (3) was calculated per new frame. Output files of aldoxime and the *HssAChE/VX* complex were visualized altogether with VMD 1.9⁴⁷ as average frames of the new ones computed through MD.

Table 1. Molecular structures of ligands predicted through protonation analysis.

Aldoxime	Structure	Percentage of the micro species ^a
4-PA		96.87%
2-PAM		97.65%
Obidoxime		93.45%
Hybrid 5C		99.74%
Obidoxime deprotonated ^b		6.44%
Hybrid 5C deprotonated ^b		0.21%

^aCalculated through Chemicalize web-based resource (<https://chemicalize.com/welcome>)⁵⁹.

^bDeprotonated ligands considered to figure out better NACs⁶.

3. Results and discussion

3.1. Modeling of the oximes and the receptor

The prevalent micro species calculated at pH = 7.4 for 4-PA, obidoxime and hybrid 5C are the ones with the oxime group protonated, while for 2-PAM, it is the oximate (Table 1). All these prevalent forms were chosen for the further molecular modelling studies. For obidoxime and hybrid 5C, however, we also decided to run the theoretical studies with the deprotonated forms, because, even knowing that these micro species are unlikely under physiological conditions, it is likely that they can be formed inside the enzyme due to proton exchange with some amino acid⁵. Accordingly, the 3D structures of each ligand in Table 1 were built through the software PC Spartan Pro 1.0.5¹⁵, and submitted to the docking and MD studies.

Superposition, with SPDBViewer[®], of the main chains of the optimized model of *HssAChE/XV/Hi-6* and the crystallographic structure of *HssAChE* complexed with XV and HI-6 resolved by Bester et al.⁶⁰, available in the PDB under the code 6CQW, afforded a RMSD value = 0.20 Å, with full superposition of the active site residues. This result shows that our model is basically identical to the experimental structure and validates the model for our theoretical studies.

3.2. Docking studies

Figure S1 of the Supporting Information shows the re-docking results and H-bond energies for the best-docked conformation of HI-6, as well as the superposition of its heavy atoms to the crystallographic conformation. The obtained RMSD = 0.16 nm was considered enough to validate the docking protocol once literature reports that a re-docking RMSD < 0.20 nm is considered acceptable^{20,21}.

The plots in Figure 4 show results for the % of selected poses according to the NAC approach^{5,7} and their correlation with the values of % of reactivation^{6,8} reported in Figure 1, while Table 2 shows the docking results for the best-selected poses of each oxime. As can be seen in Figure 4, a good correlation coefficient of $R^2 = 0.9937$ was achieved for the % of selected poses versus % of reactivation, excluding the outlier 4-PA, the only non-cationic aldoxime under study. The alignment of the three points of the pyridinium aldoximes is in line with the correlation of the % of selected poses with the probability to be in favorable conditions for enzyme reactivation, explained at methodology. However,

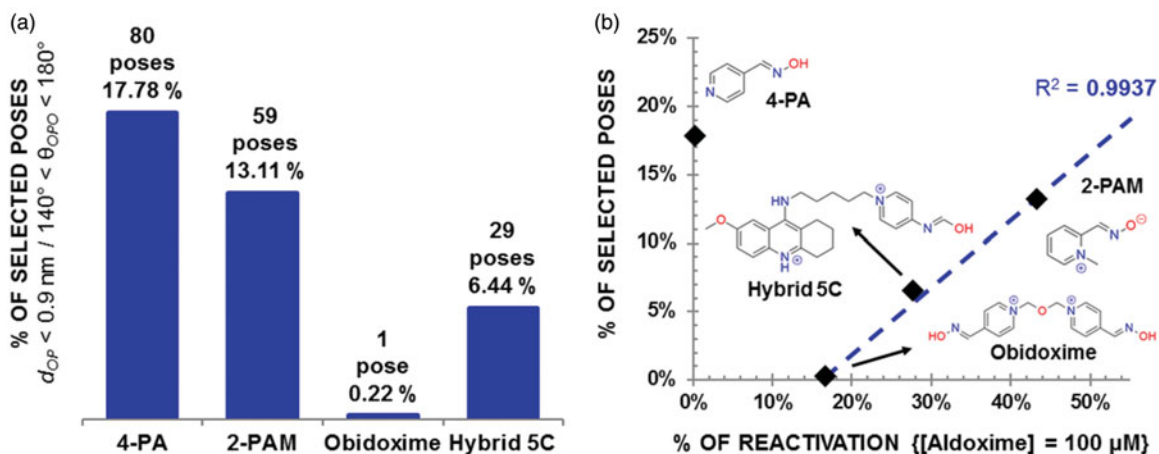


Figure 4. (a) Number of selected poses calculated for each oxime and (b) correlation between % of poses and % of reactivation.

Table 2. Docking results for poses selected for MD simulations regarding the ratio $\theta_{\text{OPo}}/d_{\text{OP}}$.

Ligand	d_{OP} (nm)	$\theta_{\text{OPo}}/d_{\text{OP}} \pm \text{SD}^{\text{a}}$ (nm^{-1})	E_{inter} (kJ/mol)	E_{Hbond} (kJ/mol)	H-bond interactions ^b	Hydrophobic interactions ($\pi-\pi$) ^{b,c}
4-PA ^d	0.81	185.19 \pm 8.37	-328.58	-18.89	Tyr124	Tyr72, Tyr124, Trp286, Phe295, Phe297, Phe299, Phe338
2-PAM ^d	0.77	190.17 \pm 6.20	-296.57	-1.49	Tyr124	Tyr72, Tyr124, Trp286, Phe295, Phe297, Phe299, Phe338, Tyr341
Obidoxime ^e	0.87	168.14	-604.94	-18.89	Tyr124, Phe297/Ser298 (Main-chain), Ser298	Tyr72, Trp86, Tyr124, Trp286, Phe295, Phe297, Phe299, Tyr337, Phe338, Tyr341
Hybrid 5C ^e	0.51	312.58 \pm 44.61	-514.65	-24.86	Tyr124, Trp286	Tyr72, Tyr124, Trp286, Phe295, Phe297, Tyr337, Phe338, Tyr341
Obidoxime deprotonated ^f	0.89	159.32	-639.46	-22.74	Tyr124, Phe297/Ser298 (Main-chain), Ser298	Tyr72, Trp86, Tyr124, Trp286, Phe295, Phe297, Phe299, Tyr337, Phe338, Tyr341
Hybrid 5C deprotonated ^f	0.47	347.10 \pm 3.80	-520.35	-5.68	Tyr124	Tyr72, Tyr124, Trp286, His287, Phe295, Phe297, Tyr337, Phe338, Tyr341

^aStandard deviation expressed as the mean of quantity of poses selected by docking studies. Not computed for the poses of obidoxime without $-\text{C}=\text{NO}^-$ moiety (only one selected pose) and obidoxime deprotonated (only four selected poses).

^bResidues in bold highlight the interactions with PAS.

^cHydrophobic interactions amongst aromatic rings in parallel.

^dAs can be seen in Figure S3 of the Supporting Information.

^eAs can be seen in Figure S4 of the Supporting Information.

^fResults of new docking studies to figure out better NACs using the deprotonated forms of obidoxime and hybrid 5C⁵, as can be seen in Table 1 and Figure S5 of the Supporting Information.

more points are needed to validate such theoretical correlation. Further calculations through our approach should be performed on a higher number of pyridinium oximes with experimental results (% of reactivation) available.

The unexpected result for 4-PA can be explained by comparison of the docking poses obtained for this ligand and 2-PAM shown in Figure S2 of the Supporting Information. Figure S2(a) Supporting Information shows that the 30 poses of 4-PA docked within residues Tyr72, Tyr124, and Trp286 of the PAS. The best among these poses, shown in Figure S3(a) Supporting Information, shows the N of the pyridine ring H-bonding with the side- and main-chains of Ser298. This pose was also sandwiched between Tyr124 and Trp286 through hydrophobic interactions, seeming to be trapped by those residues, in conjunction with Tyr72. Such interactions seem to hold 4-PA, avoiding its approach to phosphorylated Ser203. In comparison, Figure S2(b) Supporting Information shows 2 out of 30 poses of 2-PAM docked outside the PAS and Figure S3 (b) Supporting Information shows the best 2-PAM pose with a higher probability of leaving the PAS toward phosphorylated Ser203. These results suggest that interactions of the free electron pair of the pyridine ring in neutral 4-PA contribute to its trapping within the PAS, which may explain the poor reactivation shown in Figure 1. On the other hand, the quaternary N of the pyridinium ring of zwitterionic 2-PAM did not show any interaction strong enough to keep it inside the PAS.

Regarding the longer ligands, Figure S4(a) Supporting Information shows the best pose of obidoxime protonated with one oxime moiety pointed toward the VX-Ser203 adduct and the other moiety H-bonding with Ser298 and keeping the PSL inside the PAS. Similarly, Figure S5(a) Supporting Information shows the best pose of hybrid 5C protonated with 7-MEOTA stuck in the PAS and the oxime moiety H-bonding to Tyr124. In both cases, the PSL in the PAS seemed to create better stability for the nucleophilic attack against the VX-Ser203 adduct.

To figure out more refined NACs, with higher $\theta_{\text{OPo}}/d_{\text{OP}}$ ratio, new docking studies were performed on the deprotonated forms of obidoxime and hybrid 5C (Table 1). In that case, Figure S4(b) Supporting Information shows the best-evaluated pose of obidoxime deprotonated, while Figure S5(b) Supporting Information shows the best-evaluated pose of hybrid 5C deprotonated. These two poses were also selected for the MD simulations.

3.3. Molecular dynamics simulations

The MD simulations were run under periodic boundary conditions (PBC) in cubic boxes of 1060 nm^3 , filled with about 32,000 TIP4P water molecules⁴³. Five sodium ions were added to the systems with ligands 4-PA and 2-PAM and 7 to the other four systems. Two thousand, five hundred one frames were calculated from the trajectories computed for each system *HssAChE/VX/aldoxime* studied. Figures S6–S8 Supporting Information show RMSD plots suggesting stability of the systems during the 50 ns of MD simulation, considering that variations never exceeded 0.35 nm for the enzyme and 0.25 nm for each aldoxime. Analysis of the dynamical behaviour of 4-PA corroborates results from docking studies, confirming that this oxime tends to be kept stuck inside the PAS due to hydrophobic $\pi-\pi$ interactions with Tyr124 and Trp286, and H-bonds with Ser298. The d_{OP} for 4-PA increased from 0.81 nm (see Figure S3(a) Supporting Information) to around 1.1 nm in the first MD frame, and stayed at this value during the rest of the MD simulation, as shown in Supporting Information Figure S9(a). Figure S10(a) Supporting Information shows the last MD frame with 4-PA still stuck within the PAS, H-bonding to Ser298. Also, Supporting Information Figure S11 shows two H-bond interactions with both side- and main-chains of Ser298 in the PAS, in agreement with the docking results. On the other hand, the dynamical behaviour of 2-PAM suggests higher stability outside the PAS, also in agreement with the docking results. For this oxime, d_{OP} increased from 0.77 nm (see Supporting Information Figure S3(b)) to 0.9 nm in the first MD frame, staying at this value during the first half of simulation, then decreasing to 0.45 nm, until the end of the simulation, with approximation to the VX-Ser203 adduct, as shown in Supporting Information Figure S9(a). We believe that interaction with the main-chain of Phe295 around 20 ns, as shown in Supporting Information Figure S12, may have released 2-PAM from the PAS. The selected NAC for 2-PAM was the frame 1764, because of its highest ratio $\theta_{\text{OPo}}/d_{\text{OP}} = 530.303 \text{ nm}^{-1}$, with $d_{\text{OP}} = 0.33 \text{ nm}$ and $\theta_{\text{OPo}} = 175^\circ$, as can be seen in Figure 5(a).

The trapping of 4-PA within the PAS during the MD simulations, and the release of 2-PAM from the PAS toward the NAC, corroborated our findings from docking studies, also justifying the respective reactivation data shown in Figure 1 and the outlier point observed for 4-PA in Figure 4(b).

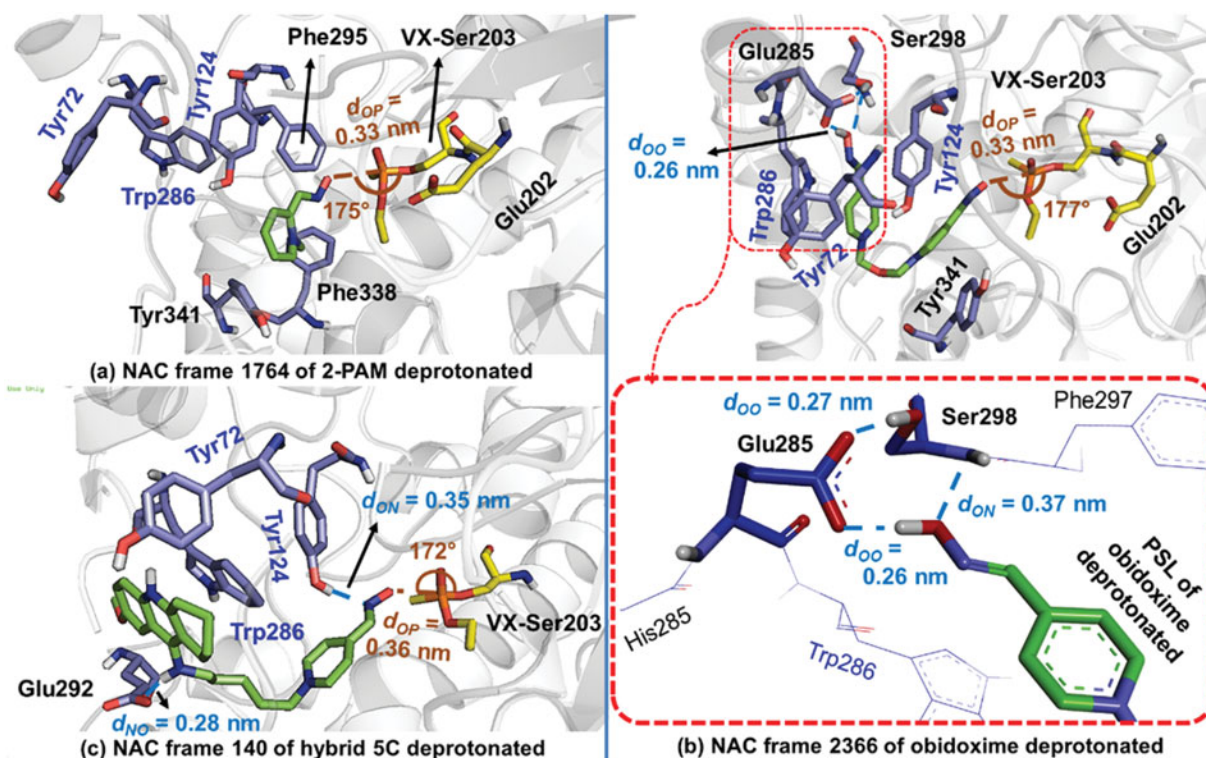


Figure 5. Comparisons amongst NAC frames of the ligands with the highest θ_{OPO}/d_{OP} .

For obidoxime, the d_{OP} first increased from 0.87 nm (Supporting Information Figure S4(a)) to around 1.0 nm in the first MD frame. Then, it decreased to around 0.4 nm, when a NAC was found within a short period around 1 ns, at frame 61, with the highest ratio $\theta_{OPO}/d_{OP} = 331.915 \text{ nm}^{-1}$ (with $d_{OP} = 0.47$ nm and $\theta_{OPO} = 156^\circ$), as shown in Supporting Information Figure S13. Subsequently, the d_{OP} has risen to around 1.4 nm, throughout the rest of simulation, as described in Supporting Information Figure S9(a). Figure S14(a,b) Supporting Information suggest that the H of the oxime group first H-bonded to the main-chain of Thr83 from 13 ns to 18 ns of MD simulation, and then, with Glu84 from around 15 ns until the end of the simulation, reinforced by the interaction between the spacer and Tyr124. Figure S10(c) Supporting Information shows the last frame with the oxime moiety interacting with Thr83 and Glu84, presenting $d_{OP} = 0.62$ nm. Likewise, Supporting Information Figures S14(c,d), and S15 show the H-bonds formed amongst the O of the oxime's PSL, the main-chain of Ser298 and the two O of Glu285, during the 50 ns of MD simulation. Such interactions seem to support the formation of the NAC at frame 61, shown in Supporting Information Figure S13.

For hybrid 5C protonated, Supporting Information Figure S16 shows the H-bond with Tyr124 during the 50 ns of simulation, as also observed in the docking study (Supporting Information Figure S5(a)), suggesting that such H-bond should keep the oxime group at a NAC. However, d_{OP} increased from 0.51 nm in the best-pose from docking, shown in Supporting Information Figure S5(a), to 1.15 nm away from the VX-Ser203 adduct, in the first MD frame. Then, it stayed at this value for the rest of the 50 ns of MD simulation, as shown in Supporting Information Figure S9(a). Moreover, Supporting Information Figure S17(a) shows H-bond between the oxime group and Thr83 for the first 10 ns of MD simulation, supported by interactions between Asp74 and Tyr341, as shown in Supporting Information Figure S10(d).

As discussed above, the NAC frame for obidoxime protonated was obtained only within a short period of roughly 1 ns and it

was not possible to find out any NAC for hybrid 5C protonated. Such findings led us to carry out more molecular modeling studies for both obidoxime and hybrid 5C deprotonated (see Table 1), as formerly discussed in docking studies.

For obidoxime deprotonated, the d_{OP} increased from 0.89 nm (Supporting Information Figure S4(b)) to roughly 1.4 nm in the first MD frame (Supporting Information Figure S9(b)). The NAC with the highest ratio $\theta_{OPO}/d_{OP} = 536.363 \text{ nm}^{-1}$ ($d_{OP} = 0.33$ nm and $\theta_{OPO} = 177^\circ$) was found out at frame 2366, within the last 4 ns of MD simulation, as shown in Figure 5(b) and Supporting Information Figure S9(b). Figure S19(a,b) Supporting Information show the interaction between the oximate group and Tyr341 that may have helped to keep the d_{OP} at 1.4 nm until 40 ns, when interaction with Tyr124 contributed to decrease d_{OP} toward the VX-Ser203 adduct. Besides, Supporting Information Figures S19(c, d) and S20, show strong interactions amongst the non-protonated PSL (the nonprotonated oxime group), Glu285 and Ser298. Such interactions may have provided more stabilization to the ligand and the decreasing of d_{OP} in the last 10 ns, as shown in Supporting Information Figures S9(b), S10(c), and S18(a). These interactions may also have provided stable conditions to achieve the NAC in the last 4 ns of MD simulation, as illustrated in Figure 5(b) and Supporting Information Figure S9(b).

Finally, in complete opposition to the other MD simulations, hybrid 5C deprotonated showed instability to stay in the gorge. However, some stability for this ligand was observed in the first 4 ns, as shown in Supporting Information Figure S8(b). The d_{OP} first increased from 0.47 nm (Supporting Information Figure S5(b)) to around 0.5 nm in the first MD frame (Supporting Information Figure S9(b)). Then, it went to about 1.0 nm, decreased to roughly 0.45 nm and then, the NAC with the highest ratio $\theta_{OPO}/d_{OP} = 477.778 \text{ nm}^{-1}$ ($d_{OP} = 0.36$ nm and $\theta_{OPO} = 172^\circ$) was found at frame 140, in which the ligand laid at a nucleophilic attack distance (Figure 5(c)). Accordingly, Supporting Information Figure S21 suggests H-bond interactions with Glu292 just in the first 4 ns, which

seemed to be interrupted close to 11 ns. Such interactions alongside hydrophobic ones with Trp286, may have provided enough stability to finally achieving a pose at the NAC. Therefore, the NAC for hybrid 5C was found only for oximate species and with the PSL outside the PAS. In terms of dynamical behaviour, the oximate group may have provided an increasing of nucleophilicity strong enough to reach the NAC. However, the 5-carbon length of its spacer is likely too long, avoiding the appropriate fitting of the PSL within the PAS. Such difficulty may not be observed for the analogues of hybrid 5C reported by Santoni et al.⁶¹ inside the crystallographic structure of *Torpedo californica* AChE (TcAChE) and docked inside VX-inhibited HssAChE. In that case, the tetrahydroacridine moiety, stabilize inside VX-inhibited HssAChE in the same way as the 7-MEOTA moiety in our study. However, the shorter spacer (4-carbon atoms) may facilitate the appropriate fitting of these molecules within the PAS to achieve the NAC.

Figure 5 shows the NAC frames of deprotonated 2-PAM, obidoxime and hybrid 5C selected with the highest ratio $\theta_{\text{OPo}}/d_{\text{OP}}$. Such selections showed a more refined conformation for nucleophilic attack with the oximate group closer to the VX-Ser203 adduct, near to the van der Waals contact ($d_{\text{OP}} < 0.4$ nm), and with more alignment amongst the O-, P-, and O- atoms. Resembling the bond to be formed in the TS ($170^\circ < \theta_{\text{OPo}} < 180^\circ$) in accordance to the definition of NAC given before¹². The values of $d_{\text{OP}} < 0.4$ nm observed can be correlated to the good reactivation results obtained by Nepovimova et al.⁶ shown in Figure 1, suggesting that these oximes are capable of reactivating VX-inhibited HssAChE because they can adopt poses at the NAC stable enough to trigger the reactivation reaction. On the other hand, the NAC frame of protonated obidoxime, shown in Supporting Information Figure S13, also with the highest $\theta_{\text{OPo}}/d_{\text{OP}}$, present a lower refinement level than its deprotonated form shown in Figure 5(b). The same Figure 5(b) details H-bond interactions inside the PAS, amongst PSL of deprotonated obidoxime, Glu285 and Ser298, which similarly took place for both ligands, crucially holding them and impeding the exit of the respective *OPAllox*, as shown in Figure 2. Accordingly, Supporting Information Figures S19(c,d) and S20 illustrate the strength of such interactions, suggesting that such *OPAllox* could be a highly potent inhibitor, sufficiently stable to re-inhibit the reactivated HssAChE, as suggested by former *in vitro* studies¹. For hybrid 5C deprotonated, the stability observed from 4 ns in Supporting Information Figure S8(b) with the d_{OP} value stuck around 0.5 nm, from 1 to 4 ns, and then continuously increasing in Supporting Information Figure S9(b), might support the exit of the respective *OPAllox* (Figure 2), after possible reactivation of the enzyme. Those chemical kinetic findings might explain the better result of reactivation for hybrid 5C than for obidoxime, despite its higher inhibition capability suggested in Figure 1.

3.4. MMPBSA results

Subsequent to MD simulations, binding energies were calculated to access more details about the dynamic behavior of the oximes. Results are shown graphically in Figure 6 and illustrated in Supporting Information Figure S22 and in Supporting Information Tables S1 and S2. Analyzing Figure 6(a) and Supporting Information Figure S22(a), we can see that Trp286 and Ser298 show significant contributions for the stabilization of 4-PA within the PAS in favor of binding. Surprisingly, the contribution from Trp286 through a hydrophobic interaction seemed to be higher than the contribution from the H-bond with Ser298, calculated by MD simulation. Accordingly, Tyr72 and Tyr124 also contributed to the stabilization of 4-PA stuck in the PAS, corroborating docking

and MD results. On the other hand, Figure 6(b) and Supporting Information Figure S22(b) and Table S1 suggest that the PAS residues do not contribute significantly for the stabilization of 2-PAM. Also, interactions with Phe338 and Tyr341 represent important contributions that might support the release of this oxime from the PAS, as pointed by the docking and MD results. Additionally, contributions from Phe337 and also the VX moiety, suggest a favorable path for the NAC. Otherwise, the less favorable contribution was from Glu202, given the positive value of $\langle \Delta H_{\text{Residue}} \rangle$. Accordingly, electrostatic interaction between Glu202 and solvent, contributes for such instability given its high $\langle \Delta G_{\text{Polar}} \rangle$, 98.26% of $\langle \Delta H_{\text{Residue}} \rangle$, as shown in Supporting Information Table S1. This finding means that such positive contribution increases the $\langle \Delta H_{\text{Binding}} \rangle$, according to Equation (4), increasing the instability of the system, and contributing to the ligand release from the PAS. Such findings for 2-PAM interactions are in line with studies on full-scope kinetic profile of interactions reported by Katalinić et al.⁶² where parameters of reactivation from the complexes *Mm*AChE/GA/pyridinium oximes were compared, considering the wild-type recombinant *Mm*AChE and selected mutants (Tyr337Ala, Tyr337Ala/Phe338Ala, Phe295Leu/Tyr337Ala, Tyr124Gln, Trp286Ala). In the case of the reactivation by 2-PAM, changes at PAS (Tyr124Gln and Trp286Ala) did not influence neither the affinity nor the reactivation⁶². Furthermore, the affinity for binding 2-PAM increased significantly, for mutant Tyr337Ala⁶². Accordingly, the presence of Tyr337 is indeed important for leading the oxime to serine reactivation^{62,63}.

For obidoxime protonated, Figure 6(c) and Supporting Information Figure S22(c) show the strongest contribution from Glu285 which, alongside Glu202, might have supported the achievement of the NAC shown in Supporting Information Figure S13, formed at the beginning of the MD simulation. Meanwhile, along with contributions from Asp74 and Glu84, the interaction with Glu285 also might have supported the deprotonation of the oxime group through interaction with Glu84, kept at an average distance of 0.25 nm from one of the O from Glu84, between 28 ns and 45 ns, as shown in Supporting Information Figure S14(b).

To hybrid 5C protonated, Figure 6(d) and Supporting Information Figure S22(d) show a significant contribution from Asp74 which is in line with the MD simulation, seeming to attract the oxime group. Such attraction might have supported the interaction with the main-chain of Thr83 kept at a mean distance of 0.32 nm, as shown in Supporting Information Figure S17(b), likely deprotonating the oxime group, analogously to deprotonated obidoxime.

For obidoxime and hybrid 5C deprotonated, only Asp74, Glu285, and Glu292 were the most significant key residues to achieve NAC for both aldoximes. Similar to 2-PAM, their weaker contributions may provide no resistance for elimination of the *OPAllox* as shown in Figure 2. In terms of chemical kinetics, such findings corroborate that the reactivation reaction through the oximate is more effective in view of lower side-chain binding contributions. In this context, Figure 6(e) and Supporting Information Figure S22(e) show that contributions from Asp74 and Glu285, are similar to protonated obidoxime and deprotonated obidoxime, although the contribution from Glu202 has not been significant for deprotonated obidoxime. Even so, the contribution from Glu285 may have been enough to support the nucleophilic attack by the oximate as discussed before and shown in Figure 5(b). Finally, Figure 6(f) and Supporting Information Figure S22(f) show the strongest contribution from Glu292 to deprotonated hybrid 5C, which corroborates the finding that its interaction with the ligand might support the nucleophilic attack, as shown in Figure 5(c). Additionally, contribution from Trp286 also seemed to

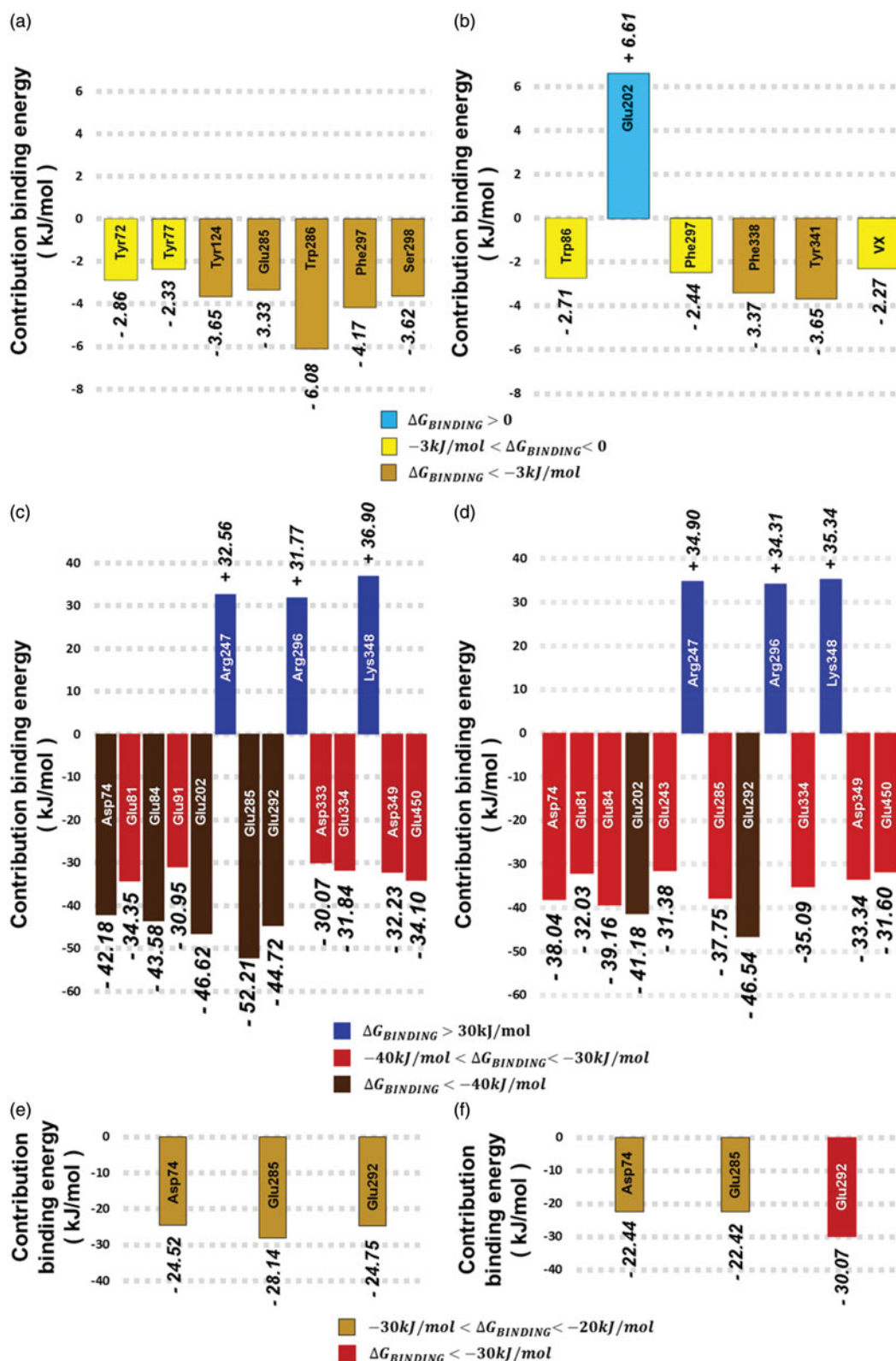


Figure 6. Comparisons amongst the most significant contributions ($\Delta H_{\text{Residue}}$) of key residues regarding the ligands (a) 4-PA, (b) 2-PAM, (c) obidoxime, (d) hybrid 5C, (e) obidoxime deprotonated, and (f) hybrid 5C deprotonated.

support such attack as shown in Figure 6(f), even not being significant like in Supporting Information Figure S22(f).

As a result, amongst the key residues illustrated in Figure 6 and Supporting Information Figure S22, contributions from Tyr341, Glu285, and Glu292 showed to be the most important for the chemical kinetics of the reactivation reaction through the

nucleophilic attack by the oximate group of 2-PAM, obidoxime and hybrid 5C, respectively. In line with the MD simulations, such results corroborate the higher potential of the oximate for reactivation, featuring a key factor for the efficacy of the reactivation^{4,5,12,13}. Such findings are also in accordance with results reported before^{4,62-64} upon docking studies of pyridinium

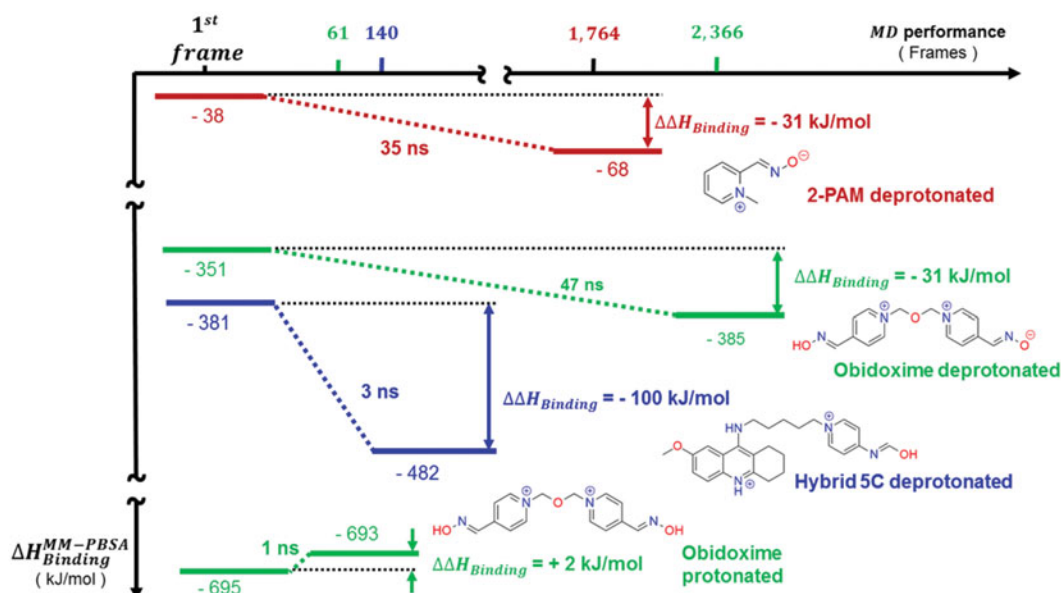


Figure 7. Binding energies computed for the NAC frames selected (Supporting Information Table S3).

aldoximes-based reactivators, pointing to Tyr72, Asp74, Tyr124, Ser198, Glu285, Trp286, and Tyr341, as key residues.

Finally, Figure 7, drawn from Supporting Information Table S3, shows $\Delta\Delta H_{\text{Binding}}$ values calculated according to Equation (6) for the NACs proposed, highlighting the most negative value for hybrid 5C deprotonated. Presumably, such comparison might support the thermodynamic viability of NAC for hybrid 5C deprotonated as a pathway toward the TS, as shown in Figure 2, regardless of further instability. Furthermore, the positive value for deprotonated obidoxime suggests more difficulty for the nucleophilic attack without the oximate. As a result, the NACs selected can be used in future studies of free energy of activation and reactivation dissociation with rate constants regarding affinity ligand–receptor, reactivity, and re-inhibition of reactivated *HssAChE* by *OPAladox*^{1,7,9}.

4. Conclusions

This work presented a NAC approach to theoretically investigate hybrid 5C as a reactivator for VX-inhibited *HssAChE*, in comparison to other aldoximes. First, a percentage of 450 poses calculated through a docking protocol was selected by geometrically limiting distance and angle of nucleophilic attack against the P of the VX-Ser203 adduct. Correlations between such theoretical percentage and data of reactivation from *in vitro* tests revealed interesting findings upon structure-activity relationship of the aldoximes studied. Then, special poses from docking studies were selected and submitted to further 50 ns of MD simulations. Finally, binding energies per amino acid residue were calculated and analysed through MM-PBSA, from the 2500 frames achieved by MD. Both poses from docking and subsequent NAC frames from MD, were selected based on the ratio $\theta_{\text{OPo}}/d_{\text{OP}}$. A more refined conformation to nucleophilic attack was figured out by such criterion, especially with the oximate group closer to phosphorylated Ser203, near to van der Waals contact ($d_{\text{OP}} < 0.4 \text{ nm}$), and with more alignment amongst the O-, P-, and O- atoms regarding the bonds to be broken and formed in the TS ($170^\circ < \theta_{\text{OPo}} < 180^\circ$). As a result, the NACs provided in this work for deprotonated 2-PAM, obidoxime and hybrid 5C, can be used in further structure activity relationship (SAR) studies regarding the reactivation reaction through a $S_{\text{N}}2$ mechanism. Meanwhile, hydrophobic and

H-bond interactions calculated through docking studies, were also compared with the ones analysed through MD simulations, allowing detailed analysis of the dynamical behaviour at the molecular level. Details about the role of the PAS for the docking of each ligand and were also discussed. Based on binding energy calculations through MM-PBSA, contributions of such interactions with key residues were evaluated regarding the stability of the complex ligand–receptor for NAC formation. As a result, amongst the key residues discussed, contributions from Glu285, Glu292, and Tyr341 showed to be the most important to provide chemical kinetic and thermodynamic conditions to the reactivation reaction by the oximate groups of 2-PAM, deprotonated obidoxime and deprotonated hybrid 5C, respectively. The molecular modeling studies presented here with the docking protocol in conjunction with MD simulations and MM-PBSA calculations, can be a powerful set of tools to help in the elucidation of the mechanism of reactivation of AChE inhibited by OPs.

Disclosure statement

No potential conflict of interest was reported by the authors.

Funding

The authors wish to thank the Military Institute of Engineering and the University of Hradec Kralové for the infrastructure, and the Brazilian financial agencies CNPq (Grant no 308225/2018–0), FAPERJ (Grant no E-02/202.961/2017), for financial support. This work was also supported by the Excellence project UHK.

ORCID

Jorge Alberto Valle da Silva <http://orcid.org/0000-0002-4297-8459>

Tanos Celmar Costa França <http://orcid.org/0000-0002-6048-8103>

References

1. Worek F, Thiermann H. The value of novel oximes for treatment of poisoning by organophosphorus compounds. *Pharmacol Ther* 2013;139:249–59.
2. Korabecny J, Soukup O, Dolezal R. From pyridinium-based to centrally active acetylcholinesterase reactivators. *Mini Rev Med Chem* 2014;14:215–21.
3. Antonijevic B, Stojiljkovic MP. Unequal efficacy of pyridinium oximes in acute organophosphate poisoning. *Clin Med Res* 2007;5:71–82.
4. Sharma R, Gupta B, Singh N, et al. Development and structural modifications of cholinesterase reactivators against chemical warfare agents in last decade: a review. *Mini Rev Med Chem* 2015;15:58–72.
5. Gorecki L, Korabecny J, Musilek K. SAR study to find optimal cholinesterase reactivator against organophosphorous nerve agents and pesticides. *Arch Toxicol* 2016;90:2831–59.
6. Nepovimova E, Korabecny J, Dolezal R, et al. 7. Methoxytacrine – 4-pyridinealoxime hybrid as novel prophylactic agent with reactivation properties in organophosphate intoxications. *Toxicol Res (Camb)* 2016;5:1012–6.
7. Sadiq SK, Coveney PV. Computing the role of near attack conformations in an enzyme-catalyzed nucleophilic bimolecular reaction. *J Chem Theory Comput* 2015;11:316–24.
8. Ellman GL, Courtney KD, Andres VJ, et al. A new and rapid colorimetric determination of acetylcholinesterase activity. *Biochem Pharmacol* 1961;7:88–95.
9. Winter M, Wille T, Musilek K, et al. Investigation of the reactivation kinetics of a large series of bispyridinium oximes with organophosphate-inhibited human acetylcholinesterase. *Toxicol Lett* 2016;244:136–42.
10. Chen Y. Beware of docking! *Trends Pharmacol Sci* 2015;36:78–95.
11. Hur S, Bruice TC. The near attack conformation approach to the study of the chorismate to prephenate reaction. *Proc Natl Acad Sci USA* 2003;100:12015–20.
12. Sahu AK, Gupta B, Sharma R, et al. Kinetic and physicochemical analysis of structurally different bis-pyridinium oximes against pesticide inhibited AChE. *Indian J Chem* 2015;4A:40–5.
13. Singh N, Karpichev Y, Tiwari AK, et al. Oxime functionality in surfactant self-assembly: an overview on combating toxicity of organophosphates. *J Mol Liq* 2015;208:237–52.
14. Deppmeier BJ, Driessen AJ, Hehre WJ, et al. PC Spartan Pro 1.0.5. Wavefunction Inc., Irvine, CA, USA; 2000.
15. Halgren TA, Nachbar RB. Merck molecular force field. IV. Conformational energies and geometries for MMFF94. *J Comput Chem* 1996;17:587–615.
16. Dewar MJS, Zoebisch EG, Healy EF, et al. AM1: a new general purpose quantum mechanical molecular model. *J Am Chem Soc* 1985;107:3902–9.
17. Bayly CI, Cieplak P, Cornell WD, et al. A well-behaved electrostatic potential based method using charge restraints for deriving atomic charges: the RESP model. *J Phys Chem* 1993;97:10269–80.
18. Berman HM, Westbrook J, Feng Z, et al. The protein data bank. *Nucleic Acids Res* 2000;28:235–42.
19. Artursson E, Andersson PO, Akfur C, et al. Catalytic-site conformational equilibrium in nerve-agent adducts of acetylcholinesterase: possible implications for the HI-6 antidote substrate specificity. *Biochem Pharmacol* 2013;85:1389–97.
20. BIOVIA, Dassault Systèmes. Discovery studio modeling environment. Release 4.5. Dassault Systèmes, San Diego (CA); 2015.
21. Boulet E, Lieberherr D, Tognolli M, et al. UniProtKB/Swiss-Prot, the manually annotated section of the Uniprot knowledgebase: how to use the entry view. *Methods Mol Biol* 2016;1374:23–54.
22. The UniProt Consortium. UniProt: the universal protein knowledgebase. *Nucleic Acids Res* 2017;45:D158–69.
23. Soreq H, Ben-Aziz R, Prody CA, et al. Molecular cloning and construction of the coding region for human acetylcholinesterase reveals a G + G-rich attenuating structures. *Proc Natl Acad Sci USA* 1990;87:9688–92.
24. Brooks BR, Brooks CL, Mackerell AD, et al. CHARMM: the biomolecular simulation program. *J Comput Chem* 2009;30:1545–614.
25. Best RB, Zhu X, Shim J, et al. Optimization of the additive CHARMM all-atom protein force field targeting improved sampling of the backbone ϕ , ψ and sidechain χ_1 and χ_2 dihedral angles. *J Comput Chem* 2012;8:3257–73.
26. Vorobyov IV, Anisimov VM, MacKerell AD. Jr. Polarizable empirical force field for alkanes based on the classical Drude oscillator model. *J Phys Chem B* 2005;109:18988–99.
27. Macias AT, MacKerell AD. Jr. CH/pi interactions involving aromatic amino acids: refinement of the CHARMM tryptophan force field. *J Comput Chem* 2005;26:1452–63.
28. Thomsen R, Christensen MH. MolDock: a new technique for high-accuracy molecular docking. *J Med Chem* 2006;49:3315–21.
29. Warren GL, Webster AC, Capelli AM, et al. A critical assessment of docking programs and scoring functions. *J Med Chem* 2006;49:5912–31.
30. Kuca K, Jun D, Junova L, et al. Synthesis, biological evaluation, and docking studies of novel bisquaternary aldoxime reactivators on acetylcholinesterase and butyrylcholinesterase inhibited by paraoxon. *Molecules* 2018;23:1103.
31. Ashani Y, Radic Z, Tsigelny I, et al. Taylor P amino acid residues controlling reactivation of organophosphonyl conjugates of acetylcholinesterase by mono- and bisquaternary oximes. *J Biol Chem* 1995;11:6370–80.
32. Delfino RT, Figueroa-Villar JD. Nucleophilic reactivation of sarin-inhibited acetylcholinesterase: a molecular modeling study. *J Phys Chem B* 2009;113:8402–11.
33. Wang J, Gu J, Leszczynski J, et al. Oxime-induced reactivation of sarin-inhibited AChE: a theoretical mechanisms study. *J Phys Chem B* 2007;111:2404–8.
34. Abraham MJ, Murtola T, Schulz R, et al. GROMACS: high performance simulations through multi-level parallelism from laptops to supercomputers. *SoftwareX* 2015;1–2:19–25.
35. Abraham MJ, van der Spoel D, Lindahl E, et al. The GROMACS development team. GROMACS user manual version; 2016;514.
36. Jorgensen WL, Maxwell DS, Tirado-Rives J. Development and testing of the OPLS all-atom force field on conformational energetics and properties of organic liquids. *J Am Chem Soc* 1996;118:11225–36.
37. da Silva AWS, Vranken WF. ACPYPE—antechamber python parser interface. *BMC Res Notes* 2012;5:367–8.
38. Carlson HA. Lessons learned over four benchmark exercises from the community structure-activity resource. *J Chem Inf Model* 2016;56:951–4.

39. Wang J, Wang W, Kollman PA, et al. Automatic atom type and bond type perception in molecular mechanical calculations. *J Mol Graph Model* 2006;25:247–60.
40. Ribeiro A, Horta BAC, Alencastro RB. MKTOP: a program for automatic construction of molecular topologies. *J Braz Chem Soc* 2008;9:1433–5.
41. Essmann U, Perera L, Berkowitz ML, et al. A smooth particle mesh Ewald method. *J Chem Phys* 1995;103:8577–93.
42. Guimaraes AP, Oliveira AA, Cunha EFF, et al. Analysis of *Bacillus anthracis* nucleoside hydrolase via *in silico* docking with inhibitors and molecular dynamics simulation. *J Mol Model* 2011;17:2939–51.
43. Silva ML, Goncalves AD, Batista PR, et al. Franca, TCC. Design, docking studies and molecular dynamics of new potential selective inhibitors of *Plasmodium falciparum* serine hydroxymethyltransferase. *Mol Simul* 2010;36:1–4.
44. Franca TCC, Medeiros ALR, Santos ECP, et al. A complete model of the *Plasmodium falciparum* bifunctional enzyme dihydrofolate reductase-thymidylate synthase. A model to design new antimalarials. *J Braz Chem Soc* 2004;15:450–4.
45. Berendsen HJC, Postma JPM, van Gusteren WF, et al. Molecular dynamics with coupling to an external bath. *J Chem Phys* 1984;81:3684–90.
46. Parrinello M, Rahman A. Polymorphic transitions in single crystals: a new molecular dynamics method. *J Appl Phys* 1981;52:7182–90.
47. Humphrey W, Dalke A, Schulten K. VMD: visual molecular dynamics. *J Mol Graph* 1996;14:33–8.
48. Delano WL. The PyMOL molecular graphics system. San Carlos, Palo Alto (CA): Delajno Scientific LLC; 2002.
49. Abascal JLF, Vega C. A general purpose model for the condensed phases of water: TIP4P/2005. *J Chem Phys* 2005;123:234505.
50. Homeyer N, Gohlke H. Free energy calculations by the molecular mechanics Poisson-Boltzmann surface area method. *Mol Inform* 2012;31:114–22.
51. Hansen N, van Gunsteren WF. Practical aspects of free-energy calculations: a review. *J Chem Theory Comput* 2014;10:2632–47.
52. Kumari R, Kumar R, Lynn A. g_mmpbsa-a GROMACS tool for high-throughput MM-PBSA calculations. *J Chem Inf Model* 2014;54:1951–62.
53. Kollman PA, Massova I, Reyes C, et al. Calculating structures and free energies of complex molecules: combining molecular mechanics and continuum models. *Acc Chem Res* 2000;33.
54. Genheden S, Ryde U. The MM/PBSA and MM/GBSA methods to estimate ligand-binding affinities. *Exp Opin Drug Discov* 2015;10:449–61.
55. Gallicchio E, Kubo MM, Levy RM. Enthalpy-entropy and cavity decomposition of alkane hydration free energies: numerical results and implications for theories of hydrophobic solvation. *J Phys Chem B* 2000;104:6271–85.
56. Wagoner JA, Baker NA. Assessing implicit models for nonpolar mean solvation forces: the importance of dispersion and volume terms. *Proc Natl Acad Sci USA* 2006;104:8331–6.
57. Skyner RE, McDonagh JL, Groom CR, et al. A review of methods for the calculation of solution free energies and the modelling of systems in solution. *Phys Chem Chem Phys* 2015;17:6174–91.
58. Honig B, Nicholls A. Classical electrostatics in biology and chemistry. *Science* 1995;268:1144–9.
59. Swain M. Chemicalize.org. *J Chem Inf Model* 2012;52:613–5.
60. Bester SM, Guelta MA, Cheung J, et al. Structural insights of stereospecific inhibition of human acetylcholinesterase by VX and subsequent reactivation by HI-6. *Chem Res Toxicol* 2018;31:1405.
61. Santoni G, de Sousa J, de la Mora E, et al. Structure-based optimization of nonquaternary reactivators of acetylcholinesterase inhibited by organophosphorus nerve agents. *J Med Chem* 2018;61:7630–9.
62. Katalinić M, Šinko G, Hrvat NM, et al. Oxime-assisted reactivation of tabun-inhibited acetylcholinesterase analysed by active site mutations. *Toxicology* 2018;406–407:104–13.
63. Artursson E, Akfur C, Hörnberg A, et al. Reactivation of tabun-hAChE investigated by structurally analogous oximes and mutagenesis. *Toxicology* 2009;265:108–14.
64. Wei Z, Liu Y, Wang Y. Novel nonquaternary reactivators showing reactivation efficiency for soman-inhibited human acetylcholinesterase. *Toxicol Res (Camb)* 2016;30:246.